Decoupling Cationic-Anionic Redox Processes in a Model Lirich Cathode via Operando X-ray Absorption Spectroscopy

Gaurav Assat, Antonella Iadecola, Charles Delacourt, Rémi Dedryvère, Jean-Marie Tarascon

Decoupling Cationic–Anionic Redox Processes in a Model Li-rich Cathode via Operando X-ray Absorption Spectroscopy

Journal:	*Chemistry of Materials*
Manuscript ID	cm-2017-03434e.R1
Manuscript Type:	Article
Date Submitted by the Author:	04-Oct-2017
Complete List of Authors:	Assat, Gaurav; College de France, Chimie du Solide et Energie Iadecola, Antonella; Synchrotron SOLEIL Delacourt, Charles; University of Picardie, Dedryvère, Rémi; University of Pau, IPREM/ECP UMR5254 CNRS Tarascon, Jean-Marie; College de France, Chimie du Solide et Energie

Decoupling Cationic–Anionic Redox Processes in a Model Li-rich Cathode via Operando X-ray Absorption Spectroscopy

Gaurav Assat,[1,2,3] Antonella Iadecola,[2,4] Charles Delacourt,[2,5] Rémi Dedryvère,[2,6] Jean-Marie Tarascon*,[1,2,3]

[1] Collège de France, Chimie du Solide et de l'Energie - UMR CNRS 8260, 11 Place Marcelin Berthelot, 75005 Paris, France
[2] Réseau sur le Stockage Electrochimique de l'Energie (RS2E) - FR CNRS 3459, 80039 Amiens Cedex, France
[3] UPMC Université Paris 06, Sorbonne Universités, 4 Place Jussieu, 75005 Paris, France
[4] Synchrotron SOLEIL, L'Orme des Merisiers Saint Aubin, Gif-sur-Yvette, F-91192, France
[5] Laboratoire de Réactivité et Chimie des Solides (LRCS) - UMR CNRS 7314, Université de Picardie Jules Verne, 33 rue Saint Leu, 80039 Amiens Cedex, France
[6] IPREM - UMR 5254 CNRS, Université de Pau et des Pays de l'Adour, Hélioparc, 2 Avenue Pierre Angot, 64053 Pau Cedex 9, France

*Corresponding author: J.-M. Tarascon: jean-marie.tarascon@college-de-france.fr

Abstract

The demonstration of reversible anionic redox in Li-rich layered oxides has revitalized the search for higher energy battery cathodes. To advance the fundamentals of this promising mechanism, we investigate herein the cationic–anionic redox processes in $Li_2Ru_{0.75}Sn_{0.25}O_3$ - a model Li-rich layered cathode in which Ru (cationic) and O (anionic) are the only redox-active sites. We reveal its charge compensation mechanism and local structural evolutions by applying *operando* (and complementary *ex situ*) X-ray absorption spectroscopy (XAS). Among other local effects, the anionic-oxidation-driven distortion of oxygen network around Ru atoms is thereby visualized. Oxidation of lattice oxygen is also directly proven via hard-X-ray photoelectron spectroscopy (HAXPES). Furthermore, we demonstrate a spectroscopy-driven visualization of electrochemical reaction paths, which enabled us to neatly decouple the individual cationic–anionic *dQ*/*dV* contributions during cycling. We hence establish the redox and structural origins of all *dQ*/*dV* features and demonstrate the vital role of anionic redox in hysteresis and kinetics. These fundamental insights about Li-rich systems are crucial for improving the existing anionic-redox-based cathodes and evaluating the ones being discovered rapidly.

Keywords. *Batteries, Li-rich layered oxide cathodes, Anionic redox, Operando X-ray absorption spectroscopy, Principal component analysis*

Introduction

A sustainable transition towards renewable energy and electrified transportation is being facilitated by steady improvements in rechargeable batteries, an important thrust area being their energy density. In the near future, Li-ion batteries are projected to maintain their dominance for high energy-density applications, more so if Li-rich Mn-based layered-oxide cathodes, e.g. $Li_{1.2}Ni_{0.13}Mn_{0.54}Co_{0.13}O_2$ (LR-NMC) that offer high capacities (> 300 mAh g^{-1}), are successfully commercialized.[1,2] Although these cathodes have attracted extensive academic and industrial interest, it was only lately that fundamental questions were answered regarding the origin of their excess capacity. Recent studies demonstrated the reversible redox activity of oxygen (anionic redox), initially in closely related 'model' Li-rich cathodes such as Li_2RuO_3[3–5] and Li_2IrO_3[6], that paved the way for evidencing the same in LR-NMC.[7–11] Anionic redox has thus rejuvenated the search for novel high energy cathodes by unlocking the possibility for capacity enhancement beyond what one expects solely from transition metals' (TM) redox.[12]

However, fundamental understanding of anionic redox is still nascent since isolating its effects is not straightforward in LR-NMCs, owing to their complicated charge compensation mechanism from TMs (Ni, Mn, and Co) as well as O. $Li_2Ru_{0.75}Sn_{0.25}O_3$ (LRSO) on the other hand, offers this possibility since its redox activity stems from just two species, namely Ru (cationic) and O (anionic) whereas Sn is just a spectator.[3] Moreover, this cathode emulates the electrochemical signature of LR-NMC, i.e. a staircase-like 1st charge followed by an S-shaped-sloped profile, and is structurally analogous to its Li_2MnO_3 (also expressed as $Li[Li_{1/3}Mn_{2/3}]O_2$) component. These peculiarities, plus a large reversible capacity (~250 mAh g^{-1}) with long cyclability[3,13,14], make LRSO a powerful model for the Li-rich layered-oxide class of cathodes, and we attempt herein to further advance the fundamental knowledge about the cationic–anionic charge compensation and local-structure evolutions in LRSO using *operando* (and complementary *ex situ*) X-ray absorption spectroscopy (XAS).

Concerning charge compensation, previous X-ray photoemission spectroscopy (XPS) studies (in *ex situ* conditions) proved the redox activity of Ru and lattice oxygen,[15] but doubts regarding quantification still remained because of the limited probe depth of in-house XPS. On the other hand, electron paramagnetic resonance (EPR) provided bulk sensitivity along with *operando* capability. However, a part of the electrochemical cycle yielded no paramagnetic signal, hence eluding an exhaustive quantification of cationic–anionic redox.[16] Crystal-structure-wise, *operando* X-ray diffraction (XRD) for LRSO simply evidenced the anionic-redox-driven nucleation of a disordered phase (XRD peak broadening).[3] The short-range local structure, inaccessible from XRD, thus still remains obscure and deserves greater attention since local effects, e.g. oxygen network distortion to form 'peroxo-like' species, are expected to majorly influence the electrochemical properties, such as voltage hysteresis (or path dependence), kinetics, and

voltage fade, as reported recently.[14] A technique more suitable for atomic-scale investigation is transmission electron microscopy (TEM), as successfully applied to visualize cationic migrations (in *ex situ* mode) over long cycling in order to explain voltage fade.[13] However, atomically resolved TEM visualization of the oxygen network, like neatly done in Li_2IrO_3 to spot O–O dimers[6], has not been possible in LRSO due to symmetry incompatibilities.[3] Lastly, LRSO's investigation with *operando* ^{7}Li nuclear magnetic resonance (NMR), a technique sensitive to local environments, also left open-questions about path dependence and cationic ordering.[17]

Aware of the abovementioned shortcomings and knowledge gaps, we present herein a detailed *operando* XAS investigation to track the electrochemically-driven evolutions in LRSO's electronic structure as well as its local structure. We reveal changes in the Ru oxidation state, and visualize, among other local effects, the anionic-redox-driven distortion in the oxygen network around Ru atoms that leads to short O–O distances, a result that was as of yet only theoretically envisaged for LRSO.[18] Through a chemometric methodology for XAS data analysis[19–22], which has recently been introduced to the field of Li (and Na) batteries[23–26], we neatly decouple the cationic–anionic redox reactions to explain each feature in LRSO's differential capacity (dQ/dV) curves. Moreover, we show how these findings can underscore the crucial role of anionic redox towards application-wise important properties (i.e. hysteresis and kinetics) in this model Li-rich cathode.

Results

$Li_2Ru_{0.75}Sn_{0.25}O_3$ (LRSO) powders were synthesized by a solid-state route as described previously[3], and then cast into Bellcore-type electrodes for electrochemical testing (see Methods).[27] The Ru K-edge X-ray absorption near edge structure (XANES) spectrum of the pristine electrode, recorded *ex situ* in transmission mode, is shown in Figure 1a. The rising edge is followed by two peaks, the first of which can be ascribed to the dipole allowed transition from 1*s* to 5*p* levels while the second one is dominated by single-scattering events involving the absorber and its Ru/Sn neighbors.[28] The rising edge for pristine LRSO superimposes neatly with that of two references, $Ru^{4+}O_2$ and $Li_2Ru^{4+}O_3$, thus establishing its Ru^{4+} oxidation state. Besides, the absence of a pre-edge feature indicates centrosymmetric Ru coordination.[29–31] Structure-wise, the Li_2MO_3 (M = Ru, Sn, Mn) family is made from layers of Li alternating with LiM_2 layers, the latter having edge-shared MO_6 octahedra in a honeycomb-like arrangement around the LiO_6 octahedra.[3] For Li_2RuO_3, the $LiRu_2$ honeycomb layer, illustrated in Figure 1b, shows an interesting asymmetry in the Ru hexagons such that one-third of the Ru–Ru distances are short (Ru–Ru dimers) - an arrangement only recently identified in literature using the $P2_1/m$ space group.[32,33] Ru K-edge extended X-ray absorption fine structure (EXAFS) oscillations contain

information about the neighboring atoms around Ru absorbers located in the honeycomb layer. For pristine LRSO, the magnitude of Fourier Transform of EXAFS oscillations, $|\chi(R)|$, shows three peaks (Figure 1c) of which the first one corresponds to RuO_6 octahedron (first shell), while the next two peaks come from the abovementioned asymmetric RuM_3 (M = Ru, Sn) honeycomb arrangement (second shell) involving one short and two long Ru–M distances. This local structural arrangement is fully established by modelling the EXAFS oscillations using six Ru–O (2.03 Å) distances, one short Ru–M (2.60 Å) distance and two long Ru–M (3.08 Å) distances (see Supp. Info. Table S1 for detailed fitting results). Such a clear characterization of the asymmetric RuM_3 distances using EXAFS analysis asserts this technique's superiority in determining structures at the local scale, compared to long-range techniques like XRD that missed this effect for many years. Note that our EXAFS model does not include light-weight Li, and neither do we differentiate between Ru and Sn (our model considers M = Ru) which is justified because LRSO and Li_2RuO_3 show nearly identical Fourier Transforms (see comparison in Supp. Info. Figure S1). Nevertheless, the quality of fits is excellent and the distances match with literature.[32–34] Building up from this initial XAS characterization of pristine LRSO, we next study the effect of delithiation (oxidation).

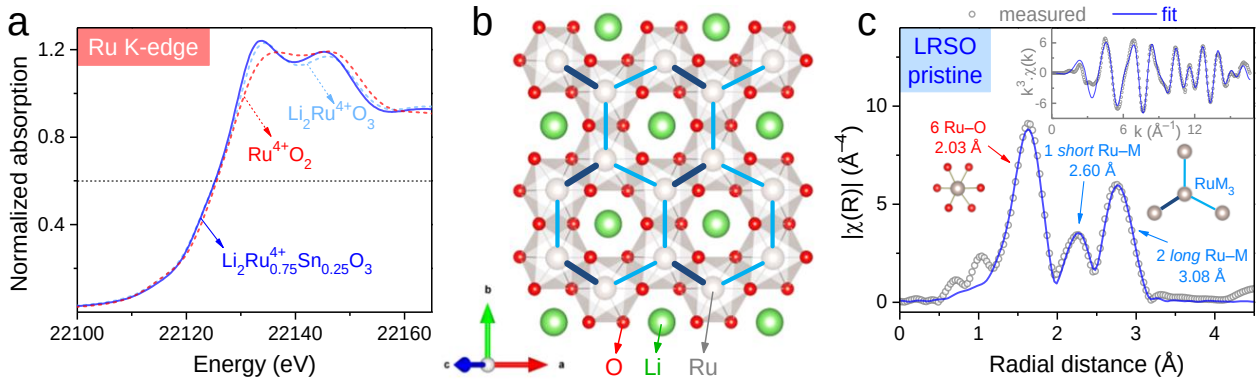

Figure 1. XAS characterization of $Li_2Ru_{0.75}Sn_{0.25}O_3$ (LRSO). (**a**) Ru K-edge XANES spectra recorded for LRSO and compared with two Ru^{4+} references. The three samples show the same edge positions (defined at jump of 0.6). (**b**) $LiRu_2$ honeycomb layer in Li_2RuO_3's crystal structure[32] showing asymmetric Ru hexagons. Short Ru–Ru dimers are represented by dark blue lines. (**c**) Magnitude of Fourier Transform of k^3-weighted EXAFS oscillations for pristine LRSO along with fitting results. The $|\chi(R)|$ plot is not corrected for phase shifts. Inset shows the fit quality in *k*-space.

Staircase-like 1st charge

An *in situ* electrochemical cell[35], equipped with two Be windows (one on either side) that allow transmission of the X-ray beam, was used for studying LRSO positive electrodes in a Li half-cell configuration. The

voltage profile measured during oxidation in such a cell features a staircase-like charging process (Figure 2a, top), replicating neatly the profile obtained with conventional coin or Swagelok cells.[3,14] Ru K-edge XAS spectra were collected in *operando* conditions without any current interruption. Each spectrum shown herein consists of data averaged over 250 seconds (500 raw scans) and the time interval between two spectra was ~20 minutes. It can be observed that the spectra evolve differently during the two voltage steps. Delithiation near 3.6 V accompanies a shift of the rising edge to higher energy by ~2 eV (Figure 2b) and an inversion of intensities of the two peaks (situated around 22135 and 22147 eV), thereby demonstrating the $Ru^{4+/5+}$ cationic redox associated with the removal of 0.75 Li^+ per formula unit of LRSO. In contrast, further oxidation at the 4.2 V plateau does not lead to an additional shift of the Ru K-edge (Figure 2c), hence signifying that the Ru^{5+} state remains unchanged and further implying the occurrence of $2O^{2-}$ / $(O_2)^{n-}$ ($n < 4$) anionic redox process as expected for charge compensation.[3] Note therefore the gradual growth of a pre-edge peak during the 4.2 V plateau. Such a pre-edge is due to the dipole-mediated 1*s*-4*d* transition that reflects the non-centrosymmetric environment of RuO_6 in the fully charged state. In fact, as already reported for 4*d* transition-metal oxides and complexes[29–31], the hybridization between the Ru 5*p* and 4*d* states becomes enhanced in a distorted octahedral coordination, leading to an increase of the pre-peak. In our case, the distortion of RuO_6 is triggered as a consequence of anionic oxidation, and similar behavior of the pre-edge was also reported for highly delithiated Li_2RuO_3.[4]

Principal component analysis (PCA)[19,23–26] results, as shown in Supp. Info. Figure S2, revealed that four principal components are needed to capture all variations in the dataset of XAS spectra measured on 1st charge. These four orthogonal components were reconstructed with the multivariate curve resolution - alternating least squares (MCR-ALS)[20–26] method such that their linear combinations attempt to simultaneously fit each complete spectrum (covering both XANES and EXAFS regions). The resulting Li-driven evolution of relative concentrations of the four components (Figure 2a, bottom) shows two separate regimes during the two voltage steps. Cationic redox (3.6 V step) involves the first three components (**I** to **II** to **III**), whereas the anionic plateau around 4.2 V involves the last two (**III** to **IV**). The XANES region of the reconstructed components shows an edge-shift from **I** to **II** to **III** (Figure 2d) and a pre-edge growth from **III** to **IV** (Figure 2e), in agreement with the cationic–anionic charge compensation mechanism discussed above.

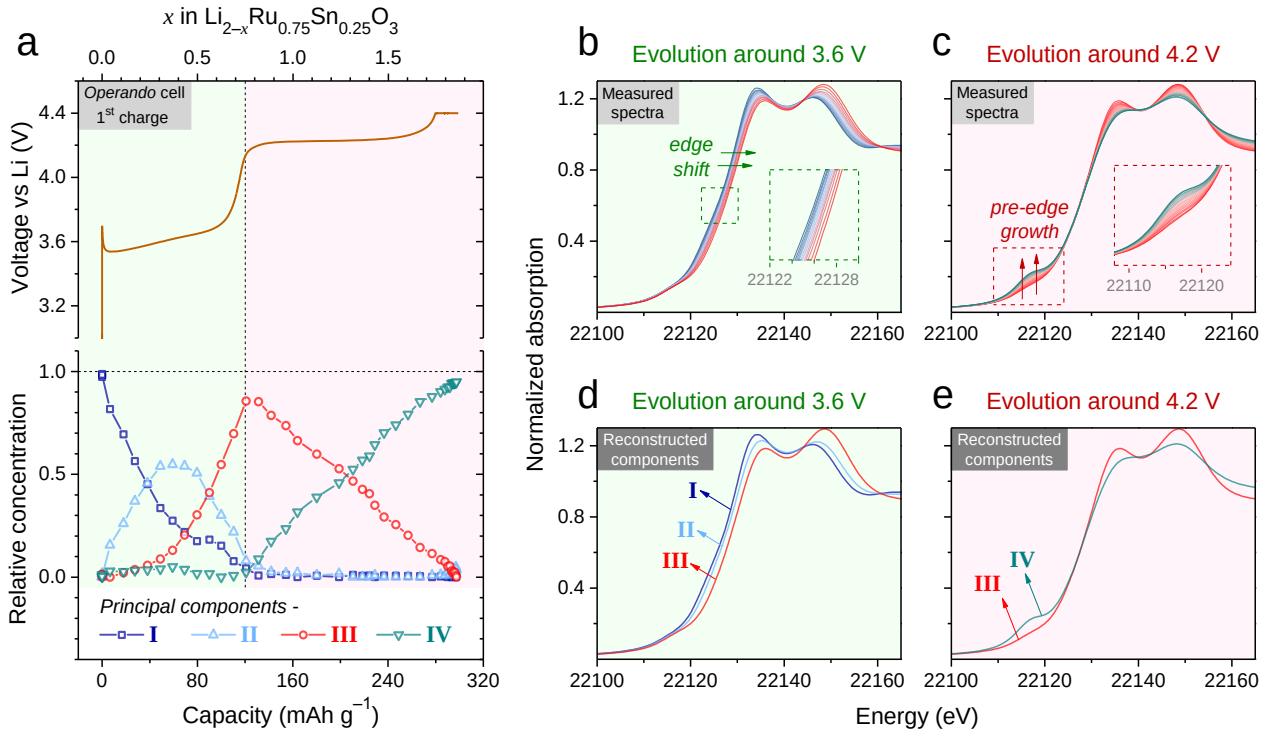

Figure 2. *Operando* XAS characterization of LRSO's 1st charge process. (**a**) The staircase-like charge voltage profile (top of figure) measured in the *operando* cell shows two steps, respectively around 3.6 V (cationic redox, green background) and 4.2 V (anionic redox, red background). Current density is 32 mA g^{-1} (C/5 for 1.0 Li^+ exchanged per formula unit). A potentiostatic hold at 4.4 V is applied till current decays to 1.6 mA g^{-1} (C/100) for achieving a full charge. The bottom of the figure tracks relative concentrations of the four principal components reconstructed using the MCR-ALS method, explaining nearly 100 % of the variance in the experimental data with the lack of fit being 0.039 %. Summation of concentrations equals unity. The evolution of Ru K-edge XANES spectra during the redox steps around (**b**) 3.6 V and (**c**) 4.2 V. Insets show enlarged views of interesting regions identified by dashed boxes. Reconstructed XANES spectra for the (**d**) first three and the (**e**) last two components.

Since XAS is a local technique, these principal components reflect the changes in short-range structure and not the long-range symmetry. EXAFS analysis of the reconstructed components was consequently carried out to track the Li-driven modifications at the local scale. For the four components, Figures 3a–d respectively show the magnitudes of Fourier Transforms of the EXAFS oscillations, $|\chi(R)|$, with their fits (see Supp. Info. Table S2 for fitting details). Component **I** (Figure 3a) is identical to the pristine LRSO electrode measured *ex situ* (recall Fig 1c), displaying three peaks in $|\chi(R)|$ as discussed before. Initial Li removal leads to the consumption of component **I** to produce **II** (Figure 2a, bottom). The $|\chi(R)|$ of component **II** is quite similar to that of **I**, such that the three peaks are still present (Figure 3b), which correspond respectively to six Ru–O (2.00 Å) distances, one short Ru–M (2.55 Å) distance and two long Ru–M (3.08 Å) distances. Initial Li removal therefore does not alter the overall local arrangement, whereas the

Ru–O shrinking supports partial $Ru^{4+/5+}$ oxidation. Further oxidation leads to the production of component **III** as **I** and **II** get consumed (Figure 2a, bottom). The local geometry of **III** is different from **I** and **II** since only two peaks feature in its $|\chi(R)|$ (Figure 3c), the first one representing six Ru–O (1.96 Å) and the second peak coming from three Ru–M (3.04 Å) neighbors. Again the shrinking of Ru–O comes as an effect of $Ru^{4+/5+}$ oxidation, whereas the merging of initially unequal Ru–M distances into a single stronger peak indicates a Li-driven rearrangement of the second shell (RuM_3), such that the irregular hexagons described in Figure 1b become regular. This justifies the symmetry change in $Li_{2-x}RuO_3$ from monoclinic (x = 0) to rhombohedral (x = 1.1) when Li is removed.[34] Moreover from the EXAFS fitting results, the shortest O–O distance in component **III** can also be estimated to be 2.48 Å since it is located at the shared edge between two RuO_6 octahedra, as schematized in Figure 3e (left side).

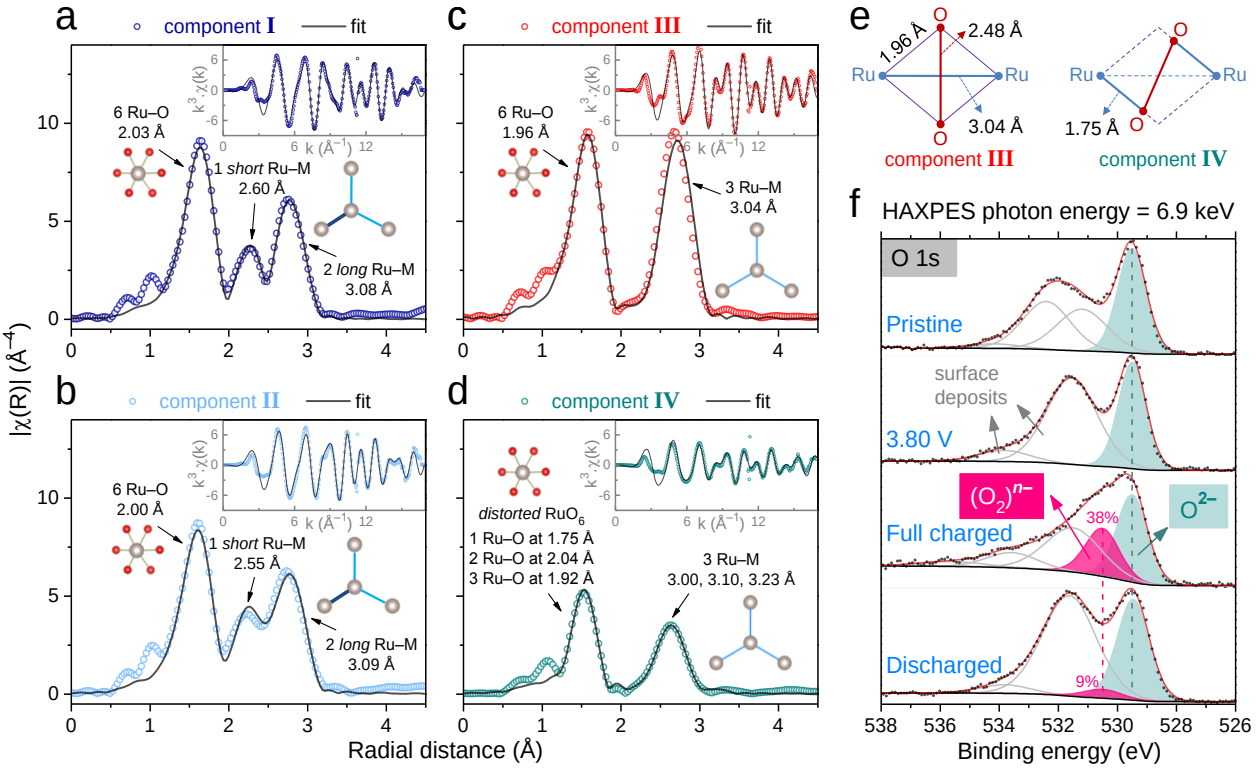

Figure 3. EXAFS analysis of principal components and HAXPES characterization of LRSO's 1st cycle. Magnitude of Fourier Transforms of k^3-weighted EXAFS oscillations for the four components (**a** to **d**) along with fitting results. The $|\chi(R)|$ plots are not corrected for phase shifts. Insets show the quality of fits in k-space. (**e**) Schematic illustrations of components **III** and **IV** (before and after anionic oxidation respectively) showing the O–O distance at the shared edge between two RuO_6 octahedra. Note that the illustration of component **IV** is not drawn to scale. (**f**) The evolution of HAXPES O 1*s* spectra of LRSO during the first cycle.

In summary, the 3.6 V cationic redox process on LRSO's 1st charge is composed of two steps, i.e. a) from **I** to **II** where the overall local arrangement having a short Ru–M distance remains intact and then b) from **II** to **III** that involves equalization of the three Ru-M distances (second shell of neighbors). Note that this mechanism is fully reproducible, as demonstrated with complementary *ex situ* XAS measurements (Supp. Info. Figure S3). Such a two-step mechanism bears a full meaning when looking at the experimental differential capacity (dQ/dV) profile around 3.6 V which also shows a double peak even at very low currents (Figure 4). A comparison of the two-step mechanism (revealed from EFAFS analysis) with the double peak in dQ/dV therefore implies that the first peak corresponds to the reaction from **I** to **II** while the second one is due to the reaction from **II** to **III**. Furthermore, for components **I**, **II**, and **III**, the amplitude of EXAFS oscillations (insets in Figure 3a–c) and consequently the intensity of $|\chi(R)|$ peaks as wells as the Debye-Waller factors (Supp. Info. Table S2) remain nearly unchanged, thus implying the preservation of structural order upon Li removal. This sheds light on previous electrochemical evidence that indicated a full reversibility of the 3.6 V cationic redox step, thereby demonstrating a classical Li-intercalation mechanism within a 'breathing' host structure.[14]

Concerning the anionic oxidation plateau, it leads to the consumption of component **III** to produce **IV**, such that both vary linearly vs. capacity which indicates the robustness of the results (Figure 2a, bottom). The $|\chi(R)|$ of **IV** (Fig 3d) shows two peaks located at similar positions as in **III**, however with a much lower intensity (thereby damped oscillations in *k*-space also, inset of Figure 3d). This indicates that the fully charged phase becomes disordered, which is also reproducibly observed with *ex situ* measurements (Supp. Info. Figure S4). This finding is in agreement with previous XRD data showing a broadening of peaks with no shifting, and supports the interpretation that a disordered phase nucleates with anionic oxidation[3], hence producing the electrochemical signature of a conversion-like mechanism.[14] EXAFS fitting of component **IV** (Figure 3d) is best achieved using a distorted RuO_6 coordination to fit the first peak, the most appropriate model having three types of Ru–O distances (1+2+3, see Supp. Info. Table S3 comparing different models considered). The second peak is fitted using three slightly dissimilar Ru–M distances. Moreover, the same model remains equally valid for the *ex situ* measured 1st charged sample (Supp. Info. Figure S4), thus strengthening its validity. The experimental observation of distorted RuO_6 octahedral coordination via EXAFS modelling is a unique finding as it was so far only a theoretical prediction[4]. Moreover, it justifies the growth of XANES pre-edge peak (Figure 1c). On the other hand, the Ru–M geometry cannot be further interpreted since the structural model is not simple, partly because of the non-quantifiable TM migration as was previously observed with TEM.[13] Nevertheless, one of the six Ru–O distances in component **IV** is significantly shorter (1.75 Å) than the rest, and we can envisage that the 'peroxo-like' oxidized-oxygen $(O–O)^{n-}$ is stabilized between two such short Ru–O distances, as

illustrated in Figure 3e (right side), consequently forming a Ru^{5+}– $(O_2)^{n-}$– Ru^{5+} entity. Experimentally evidencing this mechanism reinforces previous theoretical calculations that predicted the same.[4,18,36] Although exact estimation of the O–O distance is not trivial as several combinations are possible, but we can expect that O–O < 2.33 Å, which is significantly shorter than the 2.48 Å distance seen in component **III** before anionic oxidation (Figure 3e, left side), and signifies the 'peroxo-like' nature of oxidized oxygen.

Although a signature of oxygen oxidation can be seen on the Ru K-edge XANES via the pre-edge peak's growth, we also measured the O 1*s* photoemission spectra with bulk-sensitive hard-X-ray photoemission spectroscopy (HAXPES) for directly probing the anionic redox process (Figure 3f). The probe depth with HAXPES is significantly higher compared to classical in-house XPS due to the higher excitation photon energy (set to 6.9 keV in present work). For the O 1*s* core peak measured herein, the probe depth (defined as three times the photoelectron inelastic mean free path (IMFP) that was estimated according to the TPP-2M model[37]) is 26 nm at 6.9 keV, compared to 5.6 nm at 1.487 keV for in-house XPS. The pristine sample shows a peak at 529.5 eV that is associated with lattice oxygen O^{2-}, whereas the peaks at higher binding energy are due to oxygen-containing surface species. When LRSO is charged to 3.80 V (crossing the Ru oxidation step), no signature of anionic oxidation is observed. In contrast, fully charging to 4.4 V leads to a new oxygen environment at 530.5 eV, which is ascribed to oxidized lattice oxygen $(O_2)^{n-}$. This assignment is justified because the oxygenated surface species in the solid-electrolyte interface (SEI) layer, coming from the decomposition of electrolyte solvents and salt, are known to lie at higher binding energies.[38–40] For instance, decomposition of carbonate solvents may lead to a plenty of organic oxygenated species, but the binding energies of all such groups are observed between 531.5 and 534 eV. Similarly, inorganic species resulting from the decomposition of $LiPF_6$, e.g. phosphates, fluorophosphates $Li_xPO_yF_z$, or LiOH, are also observed at a higher binding energy than that of $(O_2)^{n-}$. Therefore the binding energy range of the oxygenated compounds found in the SEI does not overlap with O^{2-} and $(O_2)^{n-}$ peaks of the material. Moreover, a comparison of different photon energies (6.9 vs. 1.487 keV, see Supp. Info. Figure S5) shows that when probe depth is increased, the relative intensity of O 1*s* signals from the surface species decreases by a factor more than two (about 2.3) with respect to the O^{2-} component. On the contrary, the $(O_2)^{n-}/O^{2-}$ intensity ratio is not modified. The higher probe depth with HAXPES thus demonstrates the presence of $(O_2)^{n-}$ in the bulk. Since the polluting signal from surface deposits is lowered at higher photon energy, the quantification of % $(O_2)^{n-}$ is much easier with HAXPES than with in-house XPS, however the obtained % $(O_2)^{n-}$ (38 %) is similar for the two energies.[15] We also measured the O K-edge XAS spectra for $Li_{2-x}RuO_3$ in bulk-sensitive fluorescence mode (Supp. Info. Figure S6), however only qualitative interpretation is possible at this stage as supporting theoretical calculations are needed owing to the Ru–O hybridization and the particular role of oxygen non-bonding states in these materials.[18,36]

On discharge, the $(O_2)^{n-}$ peak diminishes (Figure 3f), showing the reversibility of anionic redox. The discharge voltage profile shows a sloped S-shape (Supp. Info. Figure S7) during which the capacity arises from combined cationic and anionic reductions, which are respectively located at low and high potentials, as indicated by both *operando* as well as *ex situ* XAS measurements (Supp. Info. Figures S7 and S8). EXAFS analysis shows that although the local structure after 1st discharge becomes similar to the pristine material, the disordering that was triggered by anionic oxidation is not reversed (Supp. Info. Figure S9 and Table S4). This irreversible disordering explains the permanent change of voltage profile from a staircase-like to a sloped S-shape. We next explore the cationic–anionic charge compensation mechanism once this sloped electrochemistry is stabilized during the 5th cycle.

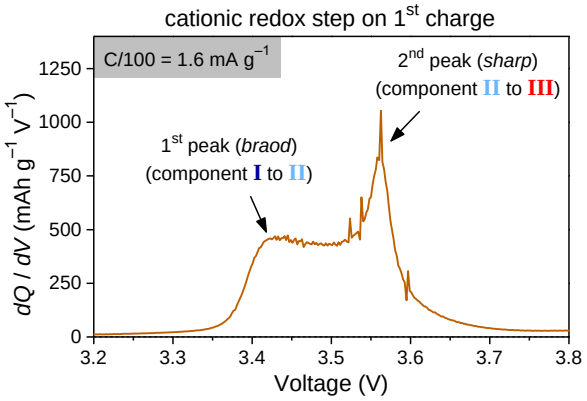

Figure 4. *dQ/dV* profile of LRSO's 1st charge recorded at a very low current of C/100 (T = 25 °C). The two peaks can be assigned to the two-step reaction mechanism revealed from PCA-MCR analysis. The C/100 profile shown displays the same features as the profile measured with a PITT protocol[14], representing the near-equilibrium potential profile.

Sloped S-shaped 5th cycle

LRSO was first activated in a regular coin cell by performing four formation cycles. The cell was then disassembled to recuperate the activated electrode, which was immediately transferred into the *operando* XAS cell for studying the 5th cycle. The electrochemical profile obtained in the *operando* cell (Figure 5a, top) is characterized by a sloped S-shape having a notable hysteresis between charge vs. discharge potentials, quite similar to that observed in coin cells[14]. The as-recorded Ru K-edge XAS spectra (measured without current interruption, time interval between two spectra was ~27 minutes) during one complete cycle show an edge shift (cationic redox) at lower potentials whereas a change in the pre-edge peak (anionic redox) at higher potentials (Supp. Info. Figure S10). Further analysis with PCA (detailed PCA results in Supp. Info. Figure S11) revealed the presence of three principal components, which were

reconstructed using the MCR-ALS method attempting to simultaneously fit all spectra measured during the 5th charge-discharge cycle. The resulting evolutions of relative concentrations of the three components as a function of capacity are shown in Figure 5a (bottom). The charging process starts with the consumption of component $\mathbf{I}_{5th}$ (*discharged*) to produce $\mathbf{II}_{5th}$ (*intermediate*). Further oxidation leads to the appearance of $\mathbf{III}_{5th}$ (*charged*) at the expense of $\mathbf{I}_{5th}$ and $\mathbf{II}_{5th}$. A reverse behavior is seen on the discharge path. Overall, the 5th cycle can hence be characterized by a sequential reaction mechanism ($\mathbf{I}_{5th}$ to $\mathbf{II}_{5th}$ to $\mathbf{III}_{5th}$ on charge and vice-versa on discharge). Note however that the profiles of relative concentrations as a function of capacity do not superimpose when compared on the charge vs. discharge paths (Figure 5a, bottom), hence demonstrating a path dependence. This explains the presence of a voltage hysteresis[14] because slightly different concentration ratios of the three reacting components would lead to slightly different electrochemical potentials.

The isolation of component $\mathbf{II}_{5th}$ (the *intermediate* species) was not trivial here as it stays far from achieving a pure relative concentration during the entire cycle, thereby underscoring the importance of PCA and MCR-ALS analyses in extracting the reaction mechanism. Further analysis of the reconstructed spectra reveals the nature of the three components. The reaction step between components $\mathbf{I}_{5th}$ and $\mathbf{II}_{5th}$ involves primarily a shift of the rising edge in the XANES part (Figure 5b), therefore meaning a change in Ru oxidation state (cationic redox). On the other hand, the main change between components $\mathbf{II}_{5th}$ and $\mathbf{III}_{5th}$ (Figure 5c) is at the pre-edge peak that arises from the distortion of oxygen network (distorted RuO_6 coordination) as a consequence of anionic oxidation, a result similar to the 1st cycle. PCA followed by MCR-ALS analysis is thus successful in decoupling the overlapping cationic–anionic redox reactions, which can in turn be individually tracked on the *dQ*/*dV* curve using a methodology schematized in Figure 5d. In short, charge compensation from the cationic redox process ($dQ_{cationic}$) is proportional to the change in concentration of component $\mathbf{I}_{5th}$ ($d[\mathbf{I}_{5th}]$) and charge compensation from the anionic redox process is proportional to the change in concentration of component $\mathbf{III}_{5th}$ ($d[\mathbf{III}_{5th}]$). The hence decoupled *dQ*/*dV* profiles (Figure 5e) clearly show how the cationic and anionic processes are separated at low and high potentials respectively, however with a considerable overlap. Moreover, summation of the two profiles can generate the overall *dQ*/*dV* profile (Figure 5e), which matches well with the as-measured *dQ*/*dV* in the *operando* cell and also resembles the profile observed in coin cells (Supp. Info. Figure S12). Such an agreement of the deconvoluted profiles with the one measured experimentally further shows the robustness of our approach. Moreover, *ex situ* measurements over the 5th cycle fully support the above identified cationic–anionic redox potentials (Supp. Info. Figure S13). Overall, our detailed XAS analysis unambiguously proves that the high potential *dQ*/*dV* peak is due to anionic redox, strengthening what was previously proposed based on EPR[16] and electrochemical measurements[14]. Furthermore, it can also be noted in Figure 5e that the cationic redox *dQ*/*dV* peaks

(centered around ~3.4 V) mirror between charge vs. discharge, unlike the anionic redox peaks (centered around ~3.8 V) that are highly asymmetric. It is this asymmetry in the anionic redox process that is responsible for voltage hysteresis. Even for *ex situ* samples (relaxed over several days) on the 5th cycle, a similar hysteresis mechanism is reproduced such that the cationic–anionic reaction extent (identified from XANES part) as well as the local structure (from EXAFS analysis) differ slightly for samples prepared at the same state of charge (SoC), i.e. with equal Li content, but via different paths - namely mid-charged vs. mid-discharged (Supp. Info. Figure S13).

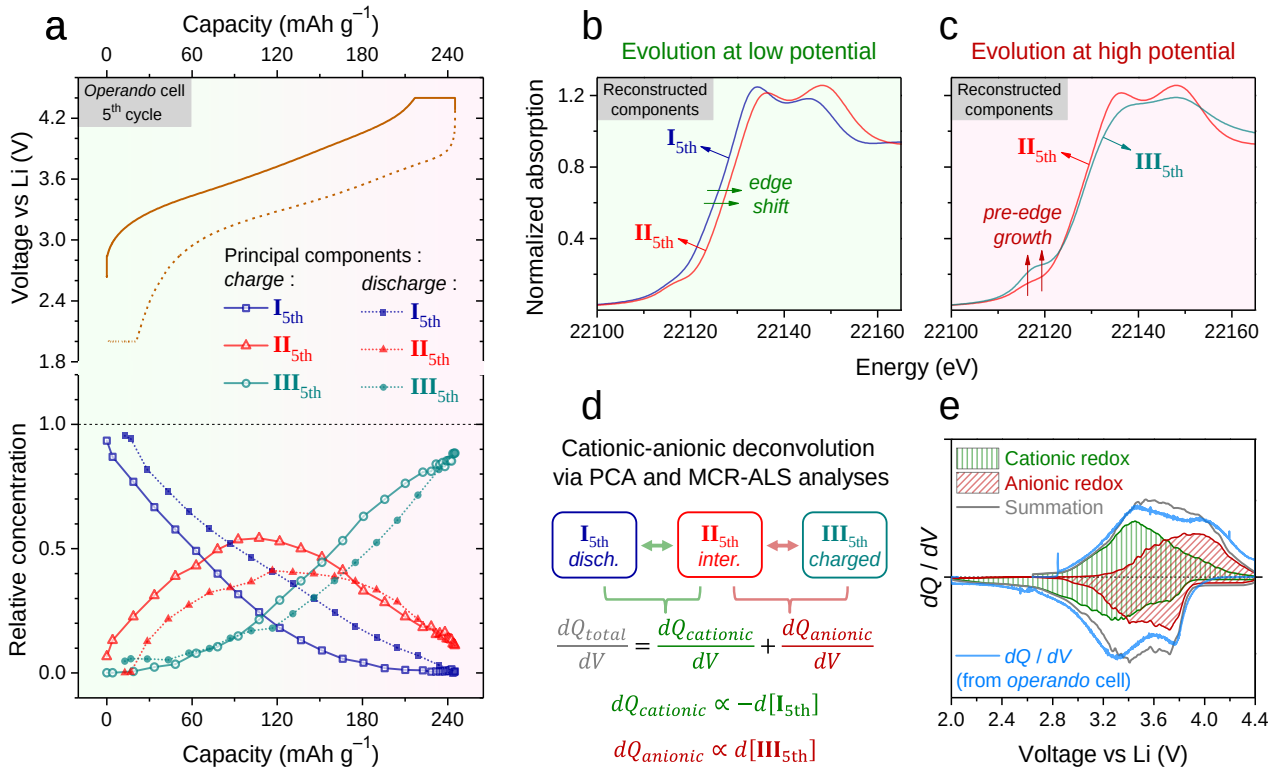

Figure 5. *Operando* XAS characterization of LRSO's 5th cycle. (**a**) The voltage profile (top part) measured in the *operando* cell with a CCCV protocol (constant current constant voltage) using a current density of 32 mA g^{-1} (C/5 for 1.0 Li$^+$ exchanged per formula unit). Potentiostatic holds at 4.4 V and 2.0 V are applied till current decays to 1.6 mA g^{-1} (C/100) for achieving a full charge and discharge. The electrode used was previously activated in a coin cell and recovered in the discharged state after four CCCV cycles. The bottom part shows the variation of relative concentrations of the three principal components as a function of capacity over the charge and discharge paths. These components, reconstructed using MCR-ALS method, explain 99.9999 % of the variance in the experimental data with the lack of fit being 0.093 %. (**b**) XANES region of the reconstructed Ru K-edge spectra comparing components **I**$_{5th}$ and **II**$_{5th}$. (**c**) Comparison of components **II**$_{5th}$ and **III**$_{5th}$. (**d**) The reaction scheme deduced from PCA followed by MCR-ALS analysis and the methodology to decouple the *dQ*/*dV* contributions of the cationic and anionic processes. (**e**) The decoupled *dQ*/*dV* profiles and their resulting summation which resembles the overall as-measured *dQ*/*dV* profile from the *operando* cell.

The local structure of the discharged state in the 5th cycle is revealed from EXAFS fitting of component $\mathbf{I}_{5th}$ (Figure 6a). It is comparable to the 1st discharged sample (recall Supp. Info. Figure S9), showing a similar arrangement as the pristine material but with increased disorder (thereby increased Debye-Waller factor also, see detailed fitting results in Supp. Info. Table S5). The three peaks in $|\chi(R)|$ correspond respectively to six Ru–O (2.04 Å) distances, one short Ru–M (2.60 Å) distance and two long Ru–M (3.09 Å) distances. Component $\mathbf{II}_{5th}$ (Figure 6b) appears similar to $\mathbf{I}_{5th}$ in terms of peak intensities and peak positions. The first peak can be modelled with a RuO_6 octahedron having minor distortion (five Ru–O distances at 1.98 Å and one at 1.85 Å, see Supp. Info. Table S6 justifying the model used). The shrinking of Ru–O when going from $\mathbf{I}_{5th}$ to $\mathbf{II}_{5th}$ comes from the cationic oxidation of Ru. One short Ru–M (2.57 Å) distance and two long Ru–M (2.75 and 3.12 Å) distances are still present in $\mathbf{II}_{5th}$. Component $\mathbf{III}_{5th}$ represents the charged state and it is more disordered than $\mathbf{I}_{5th}$ and $\mathbf{II}_{5th}$, as indicated by the reduced intensity of $|\chi(R)|$ peaks in Figure 6c as well as damped oscillations in the *k*-space (see inset). Its first peak in $|\chi(R)|$ can be modelled with a distorted RuO_6 octahedron (again using a 1+2+3 model that is appropriate for the charged material, recall Supp. Info. Table S3 for justification) and its second peak with three slightly dissimilar Ru–M distances. This local structural model is comparable to the 1st charged sample (recall Figure 3d), but with somewhat higher disorder. When comparing the Fourier Transforms, note the larger structural change during the anionic redox step between components $\mathbf{II}_{5th}$ and $\mathbf{III}_{5th}$ (Figures 6b vs. 6c) that involves a distortion of RuO_6 coordination plus a loss of order upon oxidation, compared to the less severe changes during the cationic redox step between components $\mathbf{I}_{5th}$ and $\mathbf{II}_{5th}$ (Figures 6a vs. 6b). A higher kinetic barrier can thus be envisaged for the anionic redox process, bringing a structural explanation to the recently reported sluggish electrochemical kinetics at high potentials where anionic redox is located.[14]

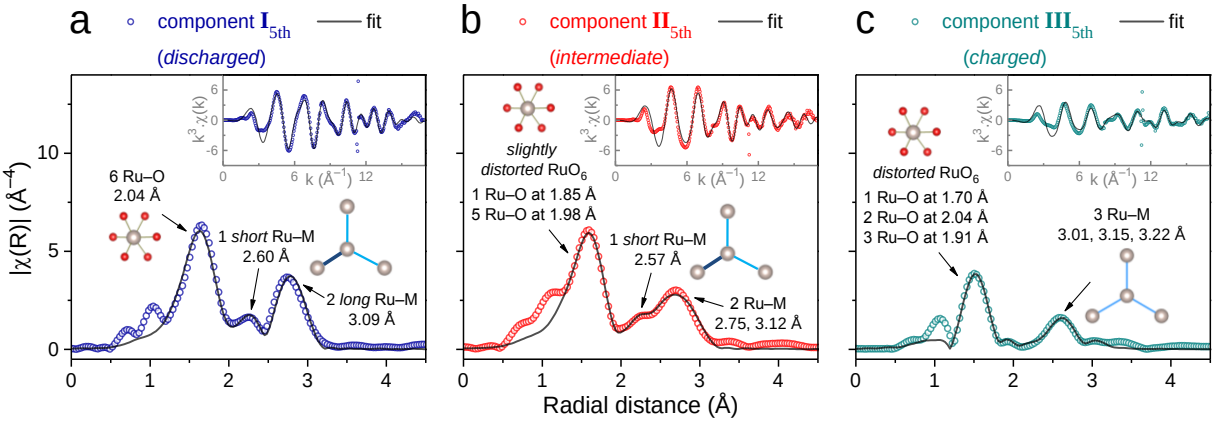

Figure 6. EXAFS analysis of principal components on the 5th cycle of LRSO. Magnitude of Fourier Transforms of k^3-weighted EXAFS oscillations for the three components (**a** to **c**) along with fitting results. The $|\chi(R)|$ plots are not corrected for phase shifts. Insets show the quality of fits in the *k*-space.

Discussion and Conclusion

Using *operando* XAS, we have studied in detail the charge compensation mechanism and local structural evolution in a model Li-rich layered oxide, $Li_2Ru_{0.75}Sn_{0.25}O_3$ (LRSO), in order to advance the fundamental understanding of cationic–anionic redox processes that govern these high capacity battery cathodes.

Starting with the analysis of pristine LRSO, we were able to neatly capture the asymmetric RuM_3 arrangement (one short and two long distances) at the local scale, an effect that is difficult to observe with long-range techniques such as XRD.[3,32,33] LRSO's staircase-like 1st charge profile, which is characteristic of Li-rich layered oxides in general[7], starts with $Ru^{4+/5+}$ cationic oxidation around 3.6 V, as characterized by the edge shift on Ru K-edge XANES spectra. Furthermore, via PCA and MCR-ALS analyses, we have shown how the cationic de-intercalation process is in fact characterized by a three-component reaction mechanism (**I** to **II** to **III**), where initial Li removal (**I** to **II**) does not alter the asymmetric RuM_3 units, whereas the completion of cationic oxidation (**II** to **III**) equalizes the RuM_3 distances, as demonstrated by EXAFS modelling of the three principal components. Note that these subtle evolutions of the local structure could not previously be detected with XRD[3], EPR[16], or NMR[17]. On the other hand, the high sensitivity of purely electrochemical methods deserves acknowledgement here since a double-peak around 3.6 V in the *dQ*/*dV* and diffusion coefficient profiles[14] had indicated the possibility of a two-step mechanism, which has now been established via *operando* XAS.

On further charging across the 4.2 V plateau, Ru does not oxidize anymore, as also confirmed by comparing with Li_3RuO_4 having a formal Ru^{5+} state (Supp. Info. Figure S4). Instead, a pre-edge peak grows in the Ru K-edge XANES, which signifies the distortion of RuO_6 coordination as a consequence of anionic oxidation. Quantification of this oxygen network distortion around Ru atoms via EXAFS modelling has in turn revealed the crucial role of short Ru–O distances in stabilizing the 'peroxo-like' oxidized-oxygen $(O–O)^{n-}$ and preventing oxygen loss. Moreover, we have also directly proven the presence of oxidized lattice oxygen in fully charged LRSO using bulk-sensitive HAXPES. Structure-wise, as the anionic oxidation process triggers severe disordering, long-range techniques like XRD cannot provide further information[3] and hence the local-scale sensitivity of XAS was valuable herein for visualizing the oxygen network distortion. This structural distortion permanently impacts the electrochemical curve on discharge, which is no longer staircase-like with disconnected cationic–anionic processes, but rather sloped S-shaped involving overlapping cationic–anionic reductions. Moreover, a full discharge cannot reinstate the pristine ordering, although the asymmetric RuM_3 arrangement reappears at the local scale.

Application-wise, it was important to study the sloped S-shaped voltage profile as it will govern the electrochemical properties of a battery with Li-rich cathodes. Via PCA and MCR-ALS analyses of the 5th cycle

operando XAS data, we established a three-component reaction mechanism ($\mathbf{I}_{5th}$ to $\mathbf{II}_{5th}$ to $\mathbf{III}_{5th}$). Through this spectroscopy-driven analysis, the overlapping cationic (at lower potential) and anionic (at higher potential) redox processes were neatly decoupled from each other by tracing their individual *dQ*/*dV* contributions. Apart from being one of the first spectroscopic demonstrations of reversibility of anionic activity in Li-rich cathodes beyond just the first couple of cycles (that are usually characterized in literature[10,12,16,17,41,42]), this work has also revealed fundamental insights about voltage hysteresis and kinetics. Concerning hysteresis in the 5th cycle, we demonstrate how the relative concentration profiles for the three components do not superimpose when compared on charge vs. discharge paths, thereby demonstrating a path-dependence. The same can alternatively be visualized from the decoupled cationic–anionic *dQ*/*dV* contributions, in which the anionic redox process displays a higher asymmetry. In light of these XAS-based results, the detrimental effect of anionic redox in triggering hysteresis when LRSO is charged to higher potentials is now fully established.[14] Note that this hysteresis mechanism is different from that of $LiFePO_4$ (non-monotonic equilibrium potential[43,44]) or conversion materials (core-shell mechanism[45] or different thermodynamic reaction paths[46]). Furthermore, there are subtle differences even for *ex situ* samples (relaxed over several days) prepared at the same SoC (or Li content) via either charge or discharge paths, which indicates the thermodynamic nature of hysteresis (independent of current). Overall, it can be concluded that the hysteresis phenomenon in Li-rich cathodes results from the interplay between the cationic–anionic redox processes which compete to compensate for the overall charge, resulting in the differences between oxidation vs. reduction paths. A similar hysteresis mechanism might be at play in LR- NMC cathodes and deserves greater attention for practically important reasons of energy efficiency and thermal management.[47–52] Concerning kinetics, the cationic reaction ($\mathbf{I}_{5th}$ to $\mathbf{II}_{5th}$) causes less severe changes to the local structure compared to the anionic one ($\mathbf{II}_{5th}$ to $\mathbf{III}_{5th}$), with the latter leading to disordering and oxygen network distortion around Ru atoms which is an energy consuming process. EXAFS analysis has therefore provided a local structural explanation behind the previously reported sluggish kinetics of the anionic redox reaction.[14]

In summary, our detailed *operando* XAS investigation of $Li_2Ru_{0.75}Sn_{0.25}O_3$ (LRSO) has revealed the fundamental Li-driven electrochemical mechanisms in this model cathode which represents the Li-rich layered oxide family. With a chemometric approach to XAS data analysis, that is based on PCA and MCR-ALS analyses, we now fully understand the charge-compensation mechanism and local structure evolutions during not just LRSO's staircase-like 1st charge but also during its more convoluted S-shaped-sloped 5th cycle. A neat decoupling of the cationic–anionic redox processes, especially on the 5th cycle, has provided structural and redox designations to different features in the *dQ*/*dV* curves, thus bridging electrochemical and spectroscopic methods. Moreover, the spectroscopic demonstration of anionic redox activity beyond just the first couple of cycles settles all doubts over its long-term reversibility. Several

extensions of this work are conceivable, ranging from further investigation of the hysteresis mechanism via half-cycles, the effect of different C-rates, and *operando* soft-XAS[53,54] measurements on Ru and oxygen, to developing multicomponent electrochemical models that incorporate the deconvoluted cationic–anionic profiles. Overall, this study demonstrates the potential of *operando* XAS, when complemented with chemometric methods, in revealing reaction intermediates, decupling overlapped reactions, and accurately tracking local structural evolutions in a non-invasive manner, making it an indispensable technique for electrochemical systems such as batteries. This calls for an improved access to synchrotron facilities as well as to XAS data analysis. As for the Li-rich cathodes, this study presents the first quantitative deconvolution of the cationic–anionic redox reactions, which could similarly be performed on LR-NMC and other high capacity anionic-redox based cathodes that are being discovered rapidly.[12] These fundamental insights about anionic-redox based electrochemical energy storage are crucial for the development of high energy density batteries.

Methods

Material synthesis and electrode preparation. Single-phase $Li_2Ru_{0.75}Sn_{0.25}O_3$ (LRSO) powders, as determined by X-ray powder diffraction (XRD) (BRUKER D8 Advance diffractometer with Cu Kα radiation, $\lambda_{K\alpha1}$=1.54056 Å, $\lambda_{K\alpha2}$=1.54439 Å), were synthesized by solid-state route, as reported previously.[3] For electrochemical testing, the powders were cast into free-standing Bellcore-type electrodes by a methodology described previously.[14,27] To obtain a good signal to noise ratio at the Ru K-edge, the active material loading in the electrode was set to ~20 mg cm^{-2}. Circular discs of ~7 mm diameter were used in each cell.

XAS sample preparation. For *ex situ* sample preparation, Swagelok-type cells were assembled in an argon glovebox (moisture and oxygen < 1ppm) with Li metal foil at the negative electrode that was separated from the LRSO positive electrode by two layers of Whatman GF/D borosilicate glass-fiber sheets acting as the separator soaked with an electrolyte – LP100 (Merck) having 1 M $LiPF_6$ dissolved in ethylene carbonate : propylene carbonate : dimethyl carbonate in a 1 : 1 : 3 weight ratio. All cells were rested for 12 hours before cycling. After charging or discharging the cells to the desired state of charge (SoC), they were carefully (avoiding short-circuit) and immediately (to avoid self-discharge under open circuit) disassembled inside an argon glovebox to recover the positive electrode. The cycled electrodes were thoroughly rinsed three times with anhydrous dimethyl carbonate (DMC) to remove the remaining electrolyte and the soluble surface deposits. DMC was evaporated by leaving the samples under vacuum (using the glovebox antechamber) for at least 1 hour. Special care was taken to never expose the samples to air or moisture. For this, they were constantly maintained in dry argon atmosphere or in vacuum. For *ex situ* XAS measurements, each cycled electrode was placed between two layers of Kapton tape, which was then sealed inside the argon glovebox within two layers of air-tight transparent plastic pouches. The pouches were taken out of the glovebox just before the XAS measurements. For *operando* XAS measurements, an *in situ* electrochemical cell[35], designed for transmission of

the X-ray beam thanks to two Be windows (one on either side), was used for studying LRSO positive electrodes in a Li half-cell configuration. The cells were assembled in an argon glovebox with identical configuration as the abovementioned Swagelok cells. The 1st cycle was studied by using a pristine electrode and the 5th cycle was studied by using an activated electrode that was previously formatted by four CCCV cycles in a coin cell. The transfer for the activated electrode was done inside the glovebox immediately after disassembling the activated coin cell.

Ru K-edge X-ray absorption spectroscopy (XAS). *Ex situ* and *operando* XAS measurements at the Ru K-edge were performed in transmission mode at the ROCK beamline[55] of synchrotron SOLEIL (France). Measurements performed in transmission mode provide bulk information averaged over many particles that are situated in the beam spot size of ~2 mm^2. A Si (220) channel-cut quick-XAS monochromator with an energy resolution of 2 eV at 22 keV was used. The intensity of the monochromatic X-ray beam was measured with three consecutive ionization detectors. The *ex situ* samples or the *operando* electrochemical cell were placed between the first and the second ionization chambers. For each measurement, successive spectra were collected at a rate of 2 Hz and averaged out over periods of 250 seconds (500 spectra) to enhance the signal to noise ratio. The time interval between two consecutive spectra in the *operando* experiments was higher (~20 minutes for the cell doing 1st cycle and ~27 minutes for the cell doing 5th cycle) since each time three different cells were simultaneously measured using a movable sample holder. Neither the current nor the acquisition was interrupted during cycling. The energy calibration was established with simultaneous absorption measurements on a RuO_2 reference placed between the second and the third ionization chambers. The data was treated using the Demeter package[56] for energy calibration and normalization. The normalized spectra were then globally analyzed with Principal component analysis (PCA)[19] in order to find the number of orthogonal components needed to describe the whole evolution during cycling. The number of principal components was then used as basis for Multivariate curve resolution - alternating least squares (MCR-ALS)[20,21] analysis using the tool developed by Jaumot et al.[22] under the constraints of i) non-negativity, and ii) closure (sum of all concentrations equals 1.00). Finally, the reconstructed components were fitted using the Artemis software.[56] Fourier Transforms of EXAFS oscillations were carried out in the *k*-range from ~4.0 to ~16 $Å^{-1}$. Fitting was performed in the *R*-range from ~1.2 to ~3.2 Å using k^3 weight. EXAFS amplitudes and phase-shifts were calculated by FEFF7 with a starting model derived from Li_2RuO_3. Conventional least squares modelling was performed using the phase and amplitude factors calculated by FEFF7. Note that the FTs throughout this work are not corrected for the phase shifts.

Hard-X-ray photoelectron spectroscopy (HAXPES). HAXPES measurements were performed on powders instead of slurry-electrodes. Li half-cells having LRSO powders ball milled with conductive Carbon Super P in a 91:09 ratio at the positive electrode (total weight kept ~40 mg for each cell to ensure repeatability) and Li metal foil at the negative electrode were assembled in Swagelok-type cells in an argon glovebox. After charging / discharging to desired SoCs, the cells were disassembled and the positive electrode powders were recovered, rinsed and dried as described above. Note that our *ex situ* electrode samples were recovered as loose powders that were thoroughly mixed. This averaged out any concentration gradients which can bias XPS results if slurry-electrodes were used instead. Great attention was paid to preserve samples from air exposure during transfer and handling. They were constantly maintained in dry argon atmosphere or in vacuum. For HAXPES, they were transferred from the argon glovebox to the beamline introduction chamber through a specially designed stainless steel transfer system (suitcase) preventing exposure to ambient.

HAXPES measurements were carried out at the GALAXIES[57] beamline of SOLEIL synchrotron in France. The photon excitation energy hν = 6.9 keV was obtained using the third order reflection of a Si(111) double-

crystal monochromator. The photoelectrons were analyzed by a SCIENTA EW4000 spectrometer, and the obtained energy resolution from the Au Fermi edge was 0.14 eV. No charge neutralizer was needed, and the pressure was kept around 10^{-8} mbar in the analysis chamber during the measurements. Experiments were carried out using the single-bunch mode (lowest synchrotron brilliance) to avoid degradation under the X-ray beam. The binding energy scale was calibrated from the C 1*s* core peak at 284.4 eV coming from Carbon Super P added to the positive electrode materials.

Supporting Information

Figures S1-S13 and Tables S1-S6. All *ex situ* Ru K-edge XAS spectra, As-recorded *operando* XAS spectra on the 1st discharge and the 5th cycle, PCA results, HAXPES vs. in-house XPS comparison, O K-edge XAS, EXAFS fitting parameters.

Author Information

*Corresponding author: J.-M. Tarascon: jean-marie.tarascon@college-de-france.fr

Notes. The authors declare no competing financial interest.

Acknowledgements

We thank K. Ramesha for providing some of the studies samples. We want also to thank the staff of the ROCK beamline (financed by the French National Research Agency (ANR) as a part of the "Investissements d'Avenir" program, reference: ANR-10-EQPX-45) and of the GALAXIES beamline of SOLEIL Synchrotron, France, for their assistance during the experiments. A.I and G.A. acknowledge the GdR C(RS)2 for the workshop organized on chemometric approach for XAS data analysis. We thank I. Pis and E. Magnano of the BACH beamline at Elettra synchrotron (Italy) for their assistance and useful advice during the soft-XAS experiments. J.M.T. and G.A. acknowledge the funding from the European Research Council (ERC) (FP/2014)/ERC Grant-Project 670116-ARPEMA.

References

1. Berg, E. J., Villevieille, C., Streich, D., Trabesinger, S. & Novák, P. Rechargeable Batteries: Grasping for the Limits of Chemistry. *J. Electrochem. Soc.* **162,** A2468–A2475 (2015).
2. Gallagher, K. G., Goebel, S., Greszler, T., Mathias, M., Oelerich, W., Eroglu, D. & Srinivasan, V. Quantifying the promise of lithium–air batteries for electric vehicles. *Energy Environ. Sci.* **7,** 1555–1563 (2014).
3. Sathiya, M., Rousse, G., Ramesha, K., Laisa, C. P., Vezin, H., Sougrati, M. T., Doublet, M.-L., Foix, D., Gonbeau, D., Walker, W., Prakash, A. S., Ben Hassine, M., Dupont, L. & Tarascon, J.-M. Reversible anionic redox chemistry in high-capacity layered-oxide electrodes. *Nat. Mater.* **12,** 827–835 (2013).
4. Li, B., Shao, R., Yan, H., An, L., Zhang, B., Wei, H., Ma, J., Xia, D. & Han, X. Understanding the Stability for Li-Rich Layered Oxide Li_2RuO_3 Cathode. *Adv. Funct. Mater.* **26,** 1330–1337 (2016).
5. Mori, D., Kobayashi, H., Okumura, T., Nitani, H., Ogawa, M. & Inaguma, Y. XRD and XAFS study on structure and cation valence state of layered ruthenium oxide electrodes, Li2RuO3 and Li2Mn0.4Ru0.6O3, upon electrochemical cycling. *Solid State Ion.* **285,** 66–74 (2016).
6. McCalla, E., Abakumov, A. M., Saubanère, M., Foix, D., Berg, E. J., Rousse, G., Doublet, M.-L., Gonbeau, D., Novák, P., Tendeloo, G. V., Dominko, R. & Tarascon, J.-M. Visualization of O-O peroxo-like dimers in high-capacity layered oxides for Li-ion batteries. *Science* **350,** 1516–1521 (2015).
7. Rozier, P. & Tarascon, J. M. Review—Li-Rich Layered Oxide Cathodes for Next-Generation Li-Ion Batteries: Chances and Challenges. *J. Electrochem. Soc.* **162,** A2490–A2499 (2015).
8. Luo, K., Roberts, M. R., Hao, R., Guerrini, N., Pickup, D. M., Liu, Y.-S., Edström, K., Guo, J., Chadwick, A. V., Duda, L. C. & Bruce, P. G. Charge-compensation in 3d-transition-metal-oxide intercalation cathodes through the generation of localized electron holes on oxygen. *Nat. Chem.* **8,** 684–691 (2016).
9. Seo, D.-H., Lee, J., Urban, A., Malik, R., Kang, S. & Ceder, G. The structural and chemical origin of the oxygen redox activity in layered and cation-disordered Li-excess cathode materials. *Nat. Chem.* **8,** 692–697 (2016).
10. Koga, H., Croguennec, L., Ménétrier, M., Mannessiez, P., Weill, F., Delmas, C. & Belin, S. Operando X-ray Absorption Study of the Redox Processes Involved upon Cycling of the Li-Rich Layered Oxide $Li_{1.20}Mn_{0.54}Co_{0.13}Ni_{0.13}O_2$ in Li Ion Batteries. *J. Phys. Chem. C* **118,** 5700–5709 (2014).
11. Koga, H., Croguennec, L., Ménétrier, M., Douhil, K., Belin, S., Bourgeois, L., Suard, E., Weill, F. & Delmas, C. Reversible oxygen participation to the redox processes revealed for Li1. 20Mn0. 54Co0. 13Ni0. 13O2. *J. Electrochem. Soc.* **160,** A786–A792 (2013).
12. Li, B. & Xia, D. Anionic Redox in Rechargeable Lithium Batteries. *Adv. Mater.* 1701054 (2017). doi:10.1002/adma.201701054
13. Sathiya, M., Abakumov, A. M., Foix, D., Rousse, G., Ramesha, K., Saubanère, M., Doublet, M. L., Vezin, H., Laisa, C. P., Prakash, A. S., Gonbeau, D., VanTendeloo, G. & Tarascon, J.-M. Origin of voltage decay in high-capacity layered oxide electrodes. *Nat. Mater.* **14,** 230–238 (2014).
14. Assat, G., Delacourt, C., Corte, D. A. D. & Tarascon, J.-M. Editors' Choice—Practical Assessment of Anionic Redox in Li-Rich Layered Oxide Cathodes: A Mixed Blessing for High Energy Li-Ion Batteries. *J. Electrochem. Soc.* **163,** A2965–A2976 (2016).
15. Foix, D., Sathiya, M., McCalla, E., Tarascon, J.-M. & Gonbeau, D. X-ray Photoemission Spectroscopy Study of Cationic and Anionic Redox Processes in High-Capacity Li-Ion Battery Layered-Oxide Electrodes. *J. Phys. Chem. C* **120,** 862–874 (2016).
16. Sathiya, M., Leriche, J.-B., Salager, E., Gourier, D., Tarascon, J.-M. & Vezin, H. Electron paramagnetic resonance imaging for real-time monitoring of Li-ion batteries. *Nat. Commun.* **6,** 6276 (2015).
17. Salager, E., Sarou-Kanian, V., Sathiya, M., Tang, M., Leriche, J.-B., Melin, P., Wang, Z., Vezin, H., Bessada, C., Deschamps, M. & Tarascon, J.-M. Solid-State NMR of the Family of Positive Electrode Materials $Li_2Ru_{1-y}Sn_yO_3$ for Lithium-Ion Batteries. *Chem. Mater.* **26,** 7009–7019 (2014).
18. Saubanère, M., McCalla, E., Tarascon, J.-M. & Doublet, M.-L. The intriguing question of anionic redox in high-energy density cathodes for Li-ion batteries. *Energy Env. Sci* **9,** 984–991 (2016).
19. Massart, D. L., Vandeginste, B. G., Buydens, L. M. C., Lewi, P. J., Smeyers-Verbeke, J. & Jong, S. D. *Handbook of Chemometrics and Qualimetrics: Part A*. (Elsevier Science Inc., 1997).
20. de Juan, A. & Tauler, R. Chemometrics applied to unravel multicomponent processes and mixtures: Revisiting latest trends in multivariate resolution. *Anal. Chim. Acta* **500,** 195–210 (2003).

21. Juan, A. de, Jaumot, J. & Tauler, R. Multivariate Curve Resolution (MCR). Solving the mixture analysis problem. *Anal. Methods* **6,** 4964–4976 (2014).
22. Jaumot, J., de Juan, A. & Tauler, R. MCR-ALS GUI 2.0: New features and applications. *Chemom. Intell. Lab. Syst.* **140,** 1–12 (2015).
23. Broux, T., Bamine, T., Simonelli, L., Stievano, L., Fauth, F., Ménétrier, M., Carlier, D., Masquelier, C. & Croguennec, L. VIV Disproportionation Upon Sodium Extraction From Na3V2(PO4)2F3 Observed by Operando X-ray Absorption Spectroscopy and Solid-State NMR. *J. Phys. Chem. C* **121,** 4103–4111 (2017).
24. C. Loaiza, L., Salager, E., Louvain, N., Boulaoued, A., Iadecola, A., Johansson, P., Stievano, L., Seznec, V. & Monconduit, L. Understanding the lithiation/delithiation mechanism of Si 1−x Ge x alloys. *J. Mater. Chem. A* **5,** 12462–12473 (2017).
25. Landa-Medrano, I., Sorrentino, A., Stievano, L., Ruiz de Larramendi, I., Pereiro, E., Lezama, L., Rojo, T. & Tonti, D. Architecture of Na-O2 battery deposits revealed by transmission X-ray microscopy. *Nano Energy* **37,** 224–231 (2017).
26. Iadecola, A., Perea, A., Aldon, L., Aquilanti, G. & Stievano, L. Li deinsertion mechanism and Jahn–Teller distortion in $LiFe_{0.75}Mn_{0.25}PO_4$: an *operando* x-ray absorption spectroscopy investigation. *J. Phys. Appl. Phys.* **50,** 144004 (2017).
27. Tarascon, J.-M., Gozdz, A. S., Schmutz, C., Shokoohi, F. & Warren, P. C. Performance of Bellcore's plastic rechargeable Li-ion batteries. *Solid State Ion.* **86,** 49–54 (1996).
28. Wu, Z., Saini, N. L., Agrestini, S., Di Castro, D., Bianconi, A., Marcelli, A., Battisti, M., Gozzi, D. & Balducci, G. Ru K-edge absorption study on the La1-xCexRu2 system. *J. Phys. Condens. Matter* **12,** 6971 (2000).
29. Getty, K., Delgado-Jaime, M. U. & Kennepohl, P. Assignment of pre-edge features in the Ru K-edge X-ray absorption spectra of organometallic ruthenium complexes. *Inorganica Chim. Acta* **361,** 1059–1065 (2008).
30. Yamamoto, T. Assignment of pre-edge peaks in K-edge x-ray absorption spectra of 3d transition metal compounds: electric dipole or quadrupole? *X-Ray Spectrom.* **37,** 572–584 (2008).
31. Aritani, H., Tanaka, T., Funabiki, T., Yoshida, S., Kudo, M. & Hasegawa, S. Structure of Mo−Mg Binary Oxides in Oxidized/Reduced States Studied by X-ray Absorption Spectroscopy at the Mo K Edge and Mg K Edge. *J. Phys. Chem.* **100,** 5440–5446 (1996).
32. Miura, Y., Yasui, Y., Sato, M., Igawa, N. & Kakurai, K. New-Type Phase Transition of Li_2RuO_3 with Honeycomb Structure. *J. Phys. Soc. Jpn.* **76,** 33705 (2007).
33. Kimber, S. A. J., Mazin, I. I., Shen, J., Jeschke, H. O., Streltsov, S. V., Argyriou, D. N., Valentí, R. & Khomskii, D. I. Valence bond liquid phase in the honeycomb lattice material Li 2 Ru O 3. *Phys. Rev. B* **89,** (2014).
34. Kobayashi, H., Kanno, R., Kawamoto, Y., Tabuchi, M., Nakamura, O. & Takano, M. Structure and lithium deintercalation of Li2−xRuO3. *Solid State Ion.* **82,** 25–31 (1995).
35. Leriche, J. B., Hamelet, S., Shu, J., Morcrette, M., Masquelier, C., Ouvrard, G., Zerrouki, M., Soudan, P., Belin, S., Elkaïm, E. & Baudelet, F. An Electrochemical Cell for Operando Study of Lithium Batteries Using Synchrotron Radiation. *J. Electrochem. Soc.* **157,** A606 (2010).
36. Xie, Y., Saubanère, M. & Doublet, M.-L. Requirements for reversible extra-capacity in Li-rich layered oxides for Li-ion batteries. *Energy Env. Sci* **10,** 266–274 (2017).
37. Tanuma, S., Powell, C. J. & Penn, D. R. Calculations of electron inelastic mean free paths. IX. Data for 41 elemental solids over the 50 eV to 30 keV range. *Surf. Interface Anal.* **43,** 689–713 (2011).
38. Dedryvère, R., Laruelle, S., Grugeon, S., Gireaud, L., Tarascon, J.-M. & Gonbeau, D. XPS Identification of the Organic and Inorganic Components of the Electrode/Electrolyte Interface Formed on a Metallic Cathode. *J. Electrochem. Soc.* **152,** A689 (2005).
39. Edström, K., Gustafsson, T. & Thomas, J. O. The cathode–electrolyte interface in the Li-ion battery. *Electrochimica Acta* **50,** 397–403 (2004).
40. Ouatani, L. E., Dedryvère, R., Siret, C., Biensan, P., Reynaud, S., Iratçabal, P. & Gonbeau, D. The Effect of Vinylene Carbonate Additive on Surface Film Formation on Both Electrodes in Li-Ion Batteries. *J. Electrochem. Soc.* **156,** A103–A113 (2009).
41. Ito, A., Sato, Y., Sanada, T., Hatano, M., Horie, H. & Ohsawa, Y. In situ X-ray absorption spectroscopic study of Li-rich layered cathode material Li[Ni0.17Li0.2Co0.07Mn0.56]O2. *J. Power Sources* **196,** 6828–6834 (2011).
42. Yu, X., Lyu, Y., Gu, L., Wu, H., Bak, S.-M., Zhou, Y., Amine, K., Ehrlich, S. N., Li, H., Nam, K.-W. & Yang, X.-Q. Understanding the Rate Capability of High-Energy-Density Li-Rich Layered $Li_{1.2}Ni_{0.15}Co_{0.1}Mn_{0.55}O_2$ Cathode Materials. *Adv. Energy Mater.* **4,** 1300950 (2014).

43. Dreyer, W., Jamnik, J., Guhlke, C., Huth, R., Moškon, J. & Gaberšček, M. The thermodynamic origin of hysteresis in insertion batteries. *Nat. Mater.* **9,** 448–453 (2010).
44. Farkhondeh, M., Pritzker, M., Fowler, M., Safari, M. & Delacourt, C. Mesoscopic modeling of Li insertion in phase-separating electrode materials: application to lithium iron phosphate. *Phys Chem Chem Phys* **16,** 22555–22565 (2014).
45. Li, L., Jacobs, R., Gao, P., Gan, L., Wang, F., Morgan, D. & Jin, S. Origins of Large Voltage Hysteresis in High-Energy-Density Metal Fluoride Lithium-Ion Battery Conversion Electrodes. *J. Am. Chem. Soc.* **138,** 2838–2848 (2016).
46. Kim, H., Kim, H., Kim, H., Kim, J., Yoon, G., Lim, K., Yoon, W.-S. & Kang, K. Understanding Origin of Voltage Hysteresis in Conversion Reaction for Na Rechargeable Batteries: The Case of Cobalt Oxides. *Adv. Funct. Mater.* **26,** 5042–5050 (2016).
47. Konishi, H., Hirano, T., Takamatsu, D., Gunji, A., Feng, X. & Furutsuki, S. Origin of hysteresis between charge and discharge processes in lithium-rich layer-structured cathode material for lithium-ion battery. *J. Power Sources* **298,** 144–149 (2015).
48. Konishi, H., Hirano, T., Takamatsu, D., Gunji, A., Feng, X., Furutsuki, S., Takahashi, S. & Terada, S. Potential hysteresis between charge and discharge reactions in Li1.2Ni0.13Mn0.54Co0.13O2 for lithium ion batteries. *Solid State Ion.* **300,** 120–127 (2017).
49. Konishi, H., Gunji, A., Feng, X. & Furutsuki, S. Effect of transition metal composition on electrochemical performance of nickel-manganese-based lithium-rich layer-structured cathode materials in lithium-ion batteries. *J. Solid State Chem.* **249,** 80–86 (2017).
50. Konishi, H., Hirano, T., Takamatsu, D., Gunji, A., Feng, X., Furutsuki, S., Okumura, T. & Terada, S. Suppression of potential hysteresis between charge and discharge reactions in lithium-rich layer-structured cathode material by increasing nickel/manganese ratio. *Solid State Ion.* **308,** 84–89 (2017).
51. Dees, D. W., Abraham, D. P., Lu, W., Gallagher, K. G., Bettge, M. & Jansen, A. N. Electrochemical Modeling and Performance of a Lithium- and Manganese-Rich Layered Transition-Metal Oxide Positive Electrode. *J. Electrochem. Soc.* **162,** A559–A572 (2015).
52. Rinaldo, S. G., Gallagher, K. G., Long, B. R., Croy, J. R., Bettge, M., Abraham, D. P., Bareño, J. & Dees, D. W. Physical Theory of Voltage Fade in Lithium-and Manganese-Rich Transition Metal Oxides. *J. Electrochem. Soc.* **162,** A897–A904 (2015).
53. Lim, J., Li, Y., Alsem, D. H., So, H., Lee, S. C., Bai, P., Cogswell, D. A., Liu, X., Jin, N., Yu, Y., Salmon, N. J., Shapiro, D. A., Bazant, M. Z., Tyliszczak, T. & Chueh, W. C. Origin and hysteresis of lithium compositional spatiodynamics within battery primary particles. *Science* **353,** 566–571 (2016).
54. Liu, X., Wang, D., Liu, G., Srinivasan, V., Liu, Z., Hussain, Z. & Yang, W. Distinct charge dynamics in battery electrodes revealed by in situ and operando soft X-ray spectroscopy. *Nat. Commun.* **4,** (2013).
55. Briois, V., Fontaine, C. L., Belin, S., Barthe, L., Moreno, T., Pinty, V., Carcy, A., Girardot, R. & Fonda, E. ROCK: the new Quick-EXAFS beamline at SOLEIL. *J. Phys. Conf. Ser.* **712,** 12149 (2016).
56. Ravel, B. & Newville, M. ATHENA, ARTEMIS, HEPHAESTUS: data analysis for X-ray absorption spectroscopy using IFEFFIT. *J. Synchrotron Radiat.* **12,** 537–541 (2005).
57. Rueff, J.-P., Ablett, J. M., Céolin, D., Prieur, D., Moreno, T., Balédent, V., Lassalle-Kaiser, B., Rault, J. E., Simon, M. & Shukla, A. The GALAXIES beamline at the SOLEIL synchrotron: inelastic X-ray scattering and photoelectron spectroscopy in the hard X-ray range. *J. Synchrotron Radiat.* **22,** 175–179 (2015).

TOC Graphic

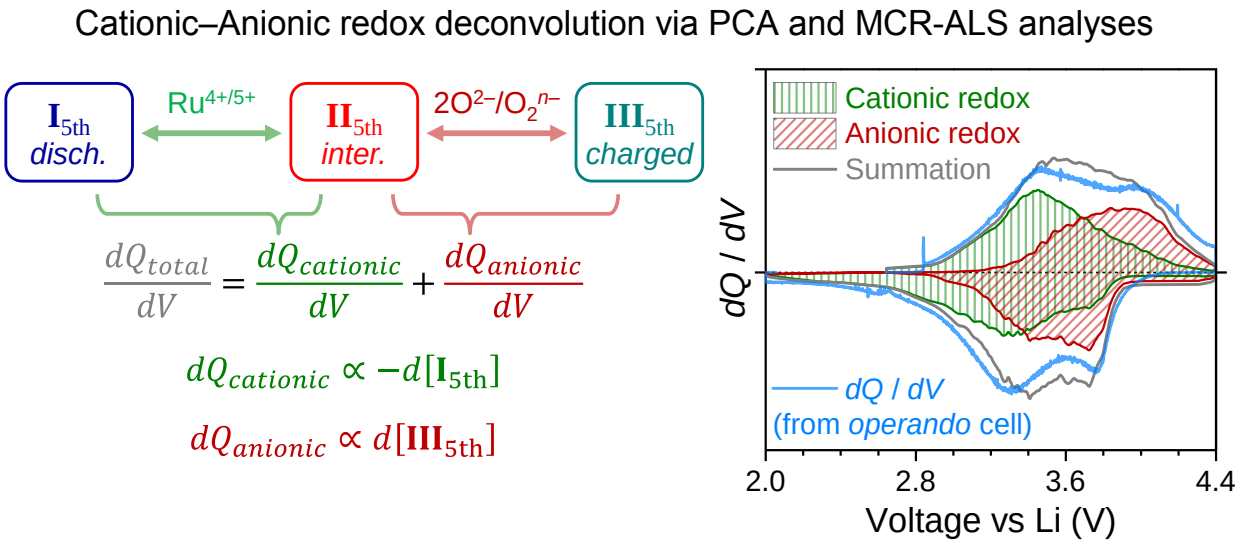
Cationic–Anionic redox deconvolution via PCA and MCR-ALS analyses
I5th disch.
Ru4+/5+
II5th inter.
2O2−/O2n−
III5th charged
dQtotal/dV = dQcationic/dV + dQanionic/dV
dQcationic ∝ −d[I5th]
dQanionic ∝ d[III5th]
Cationic redox
Anionic redox
Summation
dQ / dV
(from operando cell)
dQ / dV
2.0
2.8
3.6
4.4
Voltage vs Li (V)